Graphical Abstract

Periodic Empirical Operator Framework for Inverse Scattering and Structural Health Monitoring

R. G. Wueest, J. Mueller, J. Aichele, H. R. Thomsen

Highlights

Periodic Empirical Operator Framework for Inverse Scattering and Structural Health Monitoring

R. G. Wueest, J. Mueller, J. Aichele, H. R. Thomsen

- Presents a fully vectorized linear operator framework for inverse scattering in NDT.

- Relies solely on the principles of linear time-invariant (LTI) systems, avoiding the need for theoretical assumptions about wave propagation.

- Enforces periodic discrete time, enabling FFT-diagonalizable circular convolution operators which are solvable using the Tikhonov regularized inverse.

- Localizes sub-wavelength sized defects in both simulated aluminum plates and real-world CFRP plates.

- Post-calibration, only sparse sensor measurements are needed for rapid health monitoring.

Periodic Empirical Operator Framework for Inverse Scattering and Structural Health Monitoring

R. G. Wueest[a],[*],[1] (Researcher), J. Mueller[b] (Advisor), J. Aichele[b] (Advisor) and H. R. Thomsen[b],[2] (Advisor)

[a]*Department of Physics, ETH Zürich, 8092, Zürich, Switzerland*
[b]*Department of Earth Sciences, ETH Zürich, 8092, Zürich, Switzerland*

ABSTRACT

We present an empirical, fully vectorized linear-operator framework for first order inverse scattering and validate it experimentally on a bidirectional carbon-fiber-reinforced polymer (CFRP) plate. The framework uses bonded piezoelectric transducers to emit periodic pulses and a Laser Doppler Vibrometer (LDV) for a one-time calibration scan, constructing source–receiver impulse-response operators. By enforcing a discrete, periodic time behavior, wave propagation is modeled as a circular convolution, diagonalizable via the discrete Fourier transform (DFT). Defect localization is then formulated as a Tikhonov-regularized linear inverse problem.

After calibration, monitoring uses only sparse LDV measurements at the transducer locations. An iron cube glued to the plate serves as a defect proxy and is localized to a sub wavelength resolution. Computation cost is concentrated to the one-time calibration, whereas, subsequent evaluations require minimal data and time. If the sparse measurements are implemented using piezoelectric sensors, it could enable fully automated structural health monitoring. The empirical-operator concept may extend to alternative detection systems or unconventional sensing interfaces (e.g., touch-like surfaces). The approach is model-free and broadly applicable where forward modeling or digital-twin upkeep is impractical.

1. Introduction

Structural Health Monitoring (SHM) of engineered components seeks to localize and characterize defects before they compromise structural integrity. The relevance of SHM is closely linked to the cost of failure, which is particularly critical in aviation, and has motivated extensive research on monitoring approaches for relatively simple, flat structures [33]. Among the available techniques, piezoelectric transducers are attractive from a commercial perspective because of their low cost and ease of integration. Nevertheless, significant difficulties arise when these concepts are transferred to carbon-fiber reinforced polymers (CFRPs) [19], and a range of dedicated strategies for CFRP inspection have therefore been investigated [16, 30]. Interpreting guided-wave measurements in such materials is inherently complex: overlapping modes often demand dedicated processin—such as ridge-based time–frequency analysis, beamforming, or migration—to extract meaningful arrivals [26], while benign geometric features, multiple reflections, and mode conversions at joints and thickness transitions generate coherent clutter that can obscure damage signatures [5, 23]. These effects are amplified by the pronounced anisotropy, laminate heterogeneity, and viscoelastic damping of CFRPs, which lead to direction- and frequency-dependent dispersion and attenuation [4, 24]. Curvature, stiffeners, and adhesive interfaces introduce additional localized scattering, and in large curved assets such as rocket fuselages or wind-turbine blades, spatially varying thickness and fiber orientation challenge travel-time–based concepts [34, 8, 18, 22, 25].

Sparse monitoring of Lamb waves using a limited number of piezoelectric sensors [31] would therefore be highly attractive. However, such approaches generally rely on detailed numerical forward models. Modern numerical frameworks—including finite- and spectral-element solvers combined with higher-order plate formulations have proven capable of reproducing dispersion, mode conversion, and multi-path scattering in anisotropic laminates with high fidelity while remaining computationally efficient at ultrasonic frequencies [4, 20]. Nevertheless, such models are difficult to maintain for composite structures [29, 21]. CFRP components, in particular, exhibit variability arising from lay-up and manufacturing processes that undermines the reliability of predictive digital twins [7, 13]. In response to these limitations, data-driven strategies based on Laser Doppler Vibrometry (LDV) have gained increasing attention

as a means to capture rich wavefield information directly from the structure and to reduce dependence on uncertain a priori models [9, 27].

This paper validates a novel method based on empirical linear operators[6][17] and a fundamentally periodic time formulation. The result is a matrix based description of the system and it's inversion to solve for defects [3]. We excite the structure with bonded piezoelectric transducers and use an LDV to perform a dense, one-time calibration LDV scan that constructs source–receiver impulse-response operators. Wave propagation is treated on a discrete cyclic time axis so that it acts as circular convolution, diagonalized by the discrete Fourier transform (DFT). By designing the excitation to be strictly periodic and ensuring no other sources act on the object, the cyclic time embedding is valid by construction. We impose time periodic behavior in the setup, and thus the frequency treatment becomes equivalent to the time domain treatment. Within a single-scattering formulation, defect localization is solved via Tikhonov-regularized inverse[28][14] using only sparse monitoring data at the transducer locations. We validate the approach experimentally on an anisotropic CFRP plate, demonstrating sub-wavelength localization from sparse measurements.

2. Methodology

The test specimen is a $26.8\,\text{cm} \times 26.8 \times 0.14\,\text{cm}$ bi-directional CFRP plate (8 layers, $[0°_2/90°_2]_s$, HexPly 8552/AS4). Five low-cost brass–ceramic piezoelectric discs with a diameter of 12mm are bonded to the plate using a Crystalbond adhesive. Exact formulation and bond thickness were not recorded. As shown in Section 3.4, the method is independent of the source transfer function, and thus works for a wide range of unknown coupling properties.

The drive is a periodic pulse train with a 2 ms repetition period, using a 80 kHz Ricker wavelet as the pulse shape. An LDV scans the plate on a 104×104 square grid, recording the full 3-component velocity vector over time. For this work, we use only the out of plane Vz component, which is excited strongest by the piezoelectric sources. Figure 2 shows one frame of such a measurement. The potential use of all three velocity components is discussed in A.1.

This scan is repeated for each of the five transducers, which constitute the one-time calibration step. Data are sampled at 625 kHz and low-pass filtered to 50 kHz prior to computation. Each grid location is acquired with 10 repeats 5 separate times. I.e. we obtain 5 sets of measurements total, each having been averaged 10 times. All velocities are normalized by dividing all values by the maximum velocity recorded. The normalization increases numerical precision of floating point numbers in case of very high measurement numbers, and helps in having the optimal regularization parameter be of similar values for different systems, which will be introduced in section 3.7. As a result, the following plots such as Figure2 use unitless velocities, and may not be consistent between different plots such as Figure3b due to having a different global maxima chosen between different scripts. The normalization does not affect the results.

After calibration, a $1\,\text{cm}^3$ iron cube is bonded to the plate to simulate a defect. During monitoring, we excite each transducer again but measure only at the transducer locations. In our setup, the LDV acquires these sparse responses at the transducer positions.

For future discussion regarding sub-wavelength localization, we estimate the dispersion properties of the CFRP plate. We extract an x–t slice along the x–axis at y=0.62m through the active transducer from Figure 2 and window the time axis to exclude edge reflections (Figure 3a). We then compute a 2D FFT to obtain the k–ω spectrum. Selecting the peak-energy wavenumber $k^*(f)$ for each frequency yields the phase velocity $v_p(f) = 2\pi f / k^*(f)$ and wavelength $\lambda(f) = 2\pi / k^*(f)$ (Figure 3b). See Appendix A.4 for further comments regarding the validity of the phase velocities.

3. Mathematical framework

3.1. System assumptions

We assume: (i) linearity; (ii) time invariance; (iii) reciprocity; (iv) practical flatness (LDV access); and (v) the ability to control the excitation of the material relative to noise.

Assumptions (i), (ii), and (iii) are naturally satisfied for mechanical waves under standard conditions. Assumption (iv) refers to geometries where the object thickness is small relative to its lateral dimensions, typically valid for plate-like components such as aircraft fuselage panels and shell structures. Assumption (v) simply requires controlled excitation capability, which is standard in active NDT configurations using piezoelectric or electromagnetic transducers.
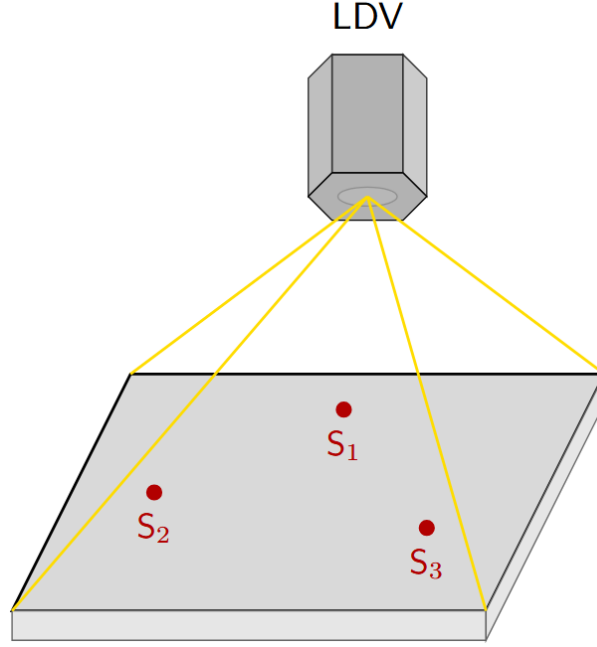
LDV

Figure 1: TODO: To be replaced with real world setup figs

3.2. Terminology and Notation

We work with discrete-time vectors and matrices throughout. The spatial domain is discretized into a set of points indexed by integers without implying any particular geometric arrangement. For instance, a 100×100 scan grid of a square plate yields 10,000 points labeled 1 through 10,000, with the specific mapping arbitrary, but fixed.

When a transducer emits a signal at location i, represented by time-domain vector $\vec{s}_i$, the observed signal $\vec{m}_j$ at location j is given by the convolution with the impulse response $\vec{g}_{ij}$ between those locations: $\vec{m}_j = \vec{g}_{ij} * \vec{s}_i$. This formulation separates spatial indices (subscripts) from the time-domain representation (vectors).

For computational implementation, these vectors correspond to discrete-time samples over a fixed acquisition window, with all operations respecting the imposed periodicity described in subsequent sections.

3.3. Periodic time and discrete representation

Repeating the excitations enforces periodicity so that the time axis can be treated on a discrete cyclic domain. Any impulse response between locations i and j is then a circular-convolution operator G_{ij}, represented by a circulant (circular Toeplitz) matrix fully determined by its first column (the sampled impulse-response vector $\vec{g}_{ij}$). Explicitly, for $\vec{g}_{ij} = (g_0, g_1, \ldots, g_{n-1})^T$,

$$G_{ij} = \begin{pmatrix} g_0 & g_{n-1} & \cdots & g_1 \\ g_1 & g_0 & \cdots & g_2 \\ \vdots & \vdots & \ddots & \vdots \\ g_{n-1} & g_{n-2} & \cdots & g_0 \end{pmatrix} \tag{1}$$

so that $G_{ij}\vec{v} = \vec{g}_{ij} * \vec{v}$ (circular convolution). All such operators are diagonalized by the discrete Fourier transform (DFT), enabling component-wise multiplication in frequency.

3.4. Empirical impulse responses

We do not separate an "ideal" injected waveform from local reverberations at a transducer. The self-measured periodic signal $\vec{s}_s$ is taken as the source vector. For a transducer s and measurement point i (grid or other transducer), the response is modeled as a circular convolution:

$$\vec{m}_i = G_{is}\vec{s}_s = g_{ij} * \vec{s}_s \tag{2}$$
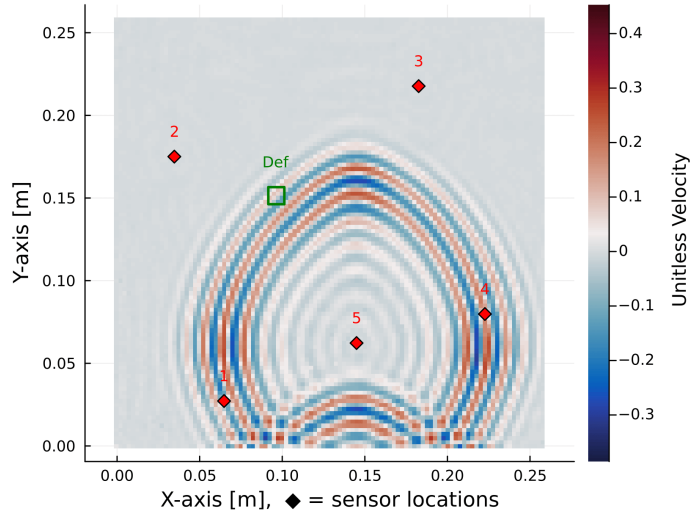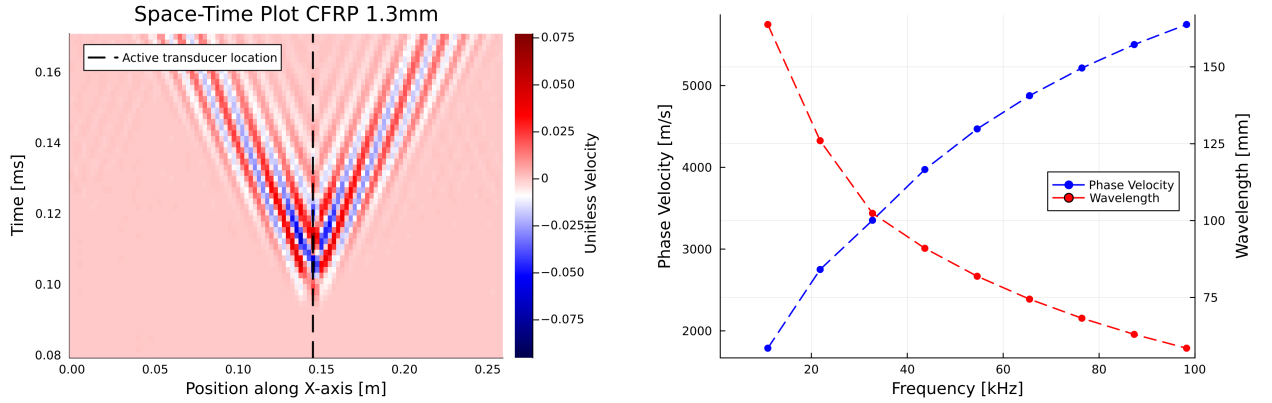
Raw data with emitter 5 at time 0.17 ms

Figure 2: Snapshot of the CFRP plate at $t = 0.17$ ms, lowpass filtered to 150 kHz. Red diamonds mark the five transducers (numbered 1–5). Transducer 5 is the active source. The green square indicates the location where the defect was bonded in the monitoring phase (not yet present in this calibration scan). Note: The results in this paper employ 1–50 kHz bandpass filtering, which significantly distorts the pulse shape compared to this view. see Appendix A.2.

(a) Space-time diagram along the y = 0.62m plane through the active sensor nr 5, derived from the same data as Figure 2.

(b) Phase velocity v_p (blue, left axis, m/s) and wavelength λ (red, right axis, mm) versus frequency f (kHz).

Figure 3: Empirical dispersion of the CFRP plate from the calibration scan.

where G_{is} is circulant (first column $\vec{g}_{is}$). Directional (mode) decomposition is intentionally omitted because the LDV records only the scalar out-of-plane velocity at each sampled point.

$\vec{g}_{ij}$ is computed as the regularized least squared solution of equation 2 of multiple sets of noisy measurements. the solution to which can be computed in the frequency domain component wise: Let $\{(\vec{s}_{s,p}, \vec{m}_{i|s,p})\}_{p=1}^{P}$ denote P repeated acquisitions. In the frequency domain (hats denote DFT components), for each frequency bin f we solve the Tikhonov-regularized least-squares problem in frequency domain:

$$\min_{\hat{g}_{is}(f)} \sum_{p=1}^{P} \left| \hat{m}_{i|s,p}(f) - \hat{s}_{s,p}(f)\hat{g}_{is}(f) \right|^2 + \alpha |\hat{g}_{is}(f)|^2 \tag{3}$$
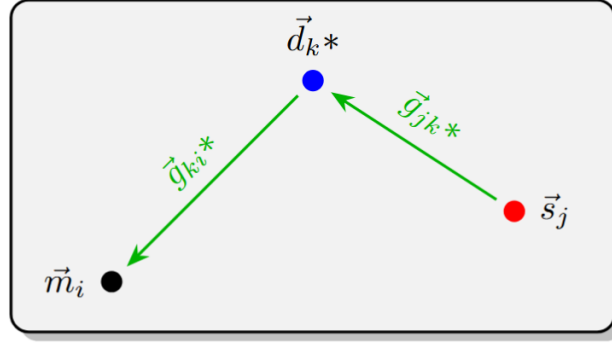
Figure 4: Visualization on how a source at location j propagates to a defect at location k, which then re-emits the wave. Afterwards, it propagates to a receiver location i. As an equation, the image visualizes $\vec{m}_i = \vec{g}_{kj} * \vec{d}_k * \vec{g}_{ik} * \vec{s}_j$.

with regularization parameter $\alpha > 0$. The closed-form solution is:

$$\hat{g}_{is}^{\text{reg}}(f) = \frac{\sum_p \overline{\hat{s}_{s,p}(f)}\,\hat{m}_{i|s,p}(f)}{\sum_p |\hat{s}_{s,p}(f)|^2 + \alpha} \tag{4}$$

The result is a stabilized impulse-response function that does not rely on assuming specific noise characteristics. α must just be a small number to assert no singularity errors happen. The exact choice does not affect the final solution in any noticeable ways.

3.5. Defect model

Since defects also satisfy the assumptions in Section 3.1, their effects can be modeled using circular convolutions. Within the single-scattering (Born-type) approximation, the scattering process is illustrated in Fig. 4. We assume a *delta-like* temporal reflection kernel, so each defect is represented by a scalar amplitude d_k at its spatial location. Algebraically, this corresponds to selecting only the first canonical temporal basis vector $\vec{d}_k = \vec{e}_0$, and physically, it corresponds to a defect position re-emitting the incoming wave immediately.

The model in general can be expanded upon to richer reflection models, with any basis of vectors as potential solutions, and has been implemented to with this capability, but no useful bases have been found (That at least justify the higher computational cost), and as such, all results shown in this paper use the simple delta basis. The generalization to richer local bases is presented in Section A.6.

3.6. Operator assembly

For an emitter at j and a measurement at i, the measured signal consists of a direct propagation term and first-order (single-scattered) contributions, as illustrated in Fig. 4:

$$\vec{m}_i = \vec{g}_{ij} * \vec{s}_j + \sum_{k=1}^{N} \vec{g}_{ik} * \vec{d}_k * \vec{g}_{kj} * \vec{s}_j. \tag{5}$$

Which can be rewritten in matrix form:

$$\vec{m}_i = G_{ij}\vec{s}_j + \sum_{k=1}^{N} G_{ik} D_k G_{kj}\vec{s}_j. \tag{6}$$

Using the commutativity of circular convolution, restate the problem as

$$\Delta\vec{m}_{ij} := \vec{m}_i - G_{ij}\vec{s}_j = \sum_{k=1}^{N}(G_{ik} G_{kj} S_j)\,\vec{d}_k. \tag{7}$$

Writing the defect vectors $\vec{d}_k$ as a single vector:

$$\mathbf{d}_{\text{full}} := \begin{bmatrix} \vec{d}_1 \\ \vec{d}_2 \\ \vdots \\ \vec{d}_N \end{bmatrix} \tag{8}$$

The problem can be restated as a general matrix problem with

$$L_{ij}^{\text{gen}} := \left[\, G_{i1}G_{1j}S_j \,\middle|\, G_{i2}G_{2j}S_j \,\middle|\, \cdots \,\middle|\, G_{iN}G_{Nj}S_j \right] \tag{9}$$

so that

$$\Delta\vec{m}_{ij} = L_{ij}^{\text{gen}}\,\mathbf{d}_{\text{full}}. \tag{10}$$

This system is typically highly underdetermined, and even when it is not, it is too large for practical computation. In our use case, the fully time-resolved defect vector would have dimension $N_{\text{grid}}N_t \approx 10^6$ (with N_{grid} spatial grid points and N_t time samples per period).

However, from the assumption that scatterers generally re-emit waves almost immediately, we can restrict the defect vectors $\vec{d}_k$ around a small set of temporal basis functions. As mentioned in the previous section, we continue with the simplest case where $\vec{d}_k = d_k * \vec{e}_0$, i.e., a 1D basis. Since every defect at any location is parameterized by a single parameter d_k, the full defect vector can be represented as

$$\mathbf{d} := \begin{bmatrix} d_1 \\ d_2 \\ \vdots \\ d_N \end{bmatrix} \tag{11}$$

and integrated into the problem by including the basis vectors into the problem:

$$L_{ij} := \left[\, G_{i1}G_{1j}S_j\vec{e}_0 \,\middle|\, G_{i2}G_{2j}S_j\vec{e}_0 \,\middle|\, \cdots \,\middle|\, G_{iN}G_{Nj}S_j\vec{e}_0 \right], \tag{12}$$

where $\vec{e}_0$ in this equation is to be understood as a column vector shaped matrix. The final problem statement for one emitter at i and sensor at j is then

$$\Delta\vec{m}_{ij} = L_{ij}\vec{\mathbf{d}}. \tag{13}$$

For multiple sensor-emitter pairs, "stacking "the selected (i, j) pairs yields the global residual system. For example for one emitter at (1) and two sensors at (2,3):

$$\vec{\mathbf{m}}_{\text{full}} = \begin{bmatrix} \Delta\vec{m}_{12} \\ \Delta\vec{m}_{13} \end{bmatrix}, \qquad L_{\text{full}} = \begin{bmatrix} L_{12} \\ L_{13} \end{bmatrix} \qquad \vec{\mathbf{m}}_{\text{full}} = L_{\text{full}}\vec{\mathbf{d}}, \tag{14}$$

Which corresponds to a [[1,2][1,3]] system.

In the examples shown in this paper in sections **??**, 5, the systems with 5 sensors are set up as [[1,2], [1,3], [1,4], [1,5], [2,3], [2,4], [2,5], [3,4], [3,5], [4,5]], effectively using 10 measurements. (Futher discussion A.7)

We have reduced the problem statement to the linear system in (14). The only approximations made are the discretization of space, the assumption of first-order scattering and immediate reflection.

3.7. Regularized inversion

Let $\mathcal{L} = L_{\text{full}}$ and $\mathbf{m} = \mathbf{m}_{\text{full}}$ from equation 14. We solve the linear inverse problem by finding $\vec{\mathbf{d}}$ to minimize following expression:

$$\text{argmin}_{\vec{\mathbf{d}}} \; \|\mathcal{L}\vec{\mathbf{d}} - \vec{\mathbf{m}}\|_2^2 + \lambda\|\Gamma\vec{\mathbf{d}}\|_2^2, \tag{15}$$

where $\Gamma \geq 0$ specifies the penalty metric (a weighting / masking matrix) and $\lambda > 0$ controls the trade-off between data fit and stabilization. The normal equations yield the closed form [1] [15]

$$\vec{\mathbf{d}} = (\mathcal{L}^T\mathcal{L} + \lambda\Gamma)^{-1}\mathcal{L}^T\vec{\mathbf{m}}. \tag{16}$$

The solution can computed directly iteratively, or by first computing the matrix $(\mathcal{L}^T\mathcal{L} + \lambda\Gamma)^{-1}\mathcal{L}^T$ (more expensive), and saving it. Allowing a rapid computation of $\vec{\mathbf{d}}$ though a matrix vector multiplication of many new measurement sets $\vec{\mathbf{m}}$.

We use Γ as a diagonal with ones everywhere except zeros at transducer locations along with a small exclusion zone around them, so those coefficients are not penalized. This allows the inversion to self-correct for slight inconsistencies in the emitter pulse form. When plotting the defect vector as a heatmap during evaluation, these regions are omitted from the plot by setting to 0, as otherwise, these regions would dominate the results.

The optimal regularization parameter λ in this paper is chosen with no particular method. In the examples of this paper, we are presenting the solution using the optimal parameters as is without discussing it. More formal methods of finding the optimal λ are explored in [2], and the exploration of the effects of different parameter choices for the presented method are documented in [32].

More advanced avenues of implementing the Tikhonov regularization are explored[14].

4. Results

Figure 5a shows the reconstructed defect vector $\vec{\mathbf{d}}$, where each pixel represents the absolute value at a spatial grid point. After solving equation 14, the resulting vector assigns a reflection amplitude to every grid point. In this case, the vector has $101 \times 104 = 10{,}816$ entries, one per grid point. For visualization, each grid point is mapped back onto the 2D plane according to its original arrangement. The heatmap displays the absolute value at each location, which can be interpreted as the amplitude with which the incoming wave is reflected. No phase information is preserved, as the vector is complex-valued. The algorithm does not know the spatial correspondence of each index, and the system is not restricted to a 2D plane.

The defect in Figure 5a is clearly localized near the target location (yellow square). Small black regions appear around each transducer (red diamonds). These exclusion zones correspond to the unpenalized region in the regularization (Section 3.7) and are masked in the visualization. Behind this mask, the heatmap would show very high values, but these mostly reflect systematic errors in the experiment setup, such as differences in pulse amplitude between calibration and monitoring.
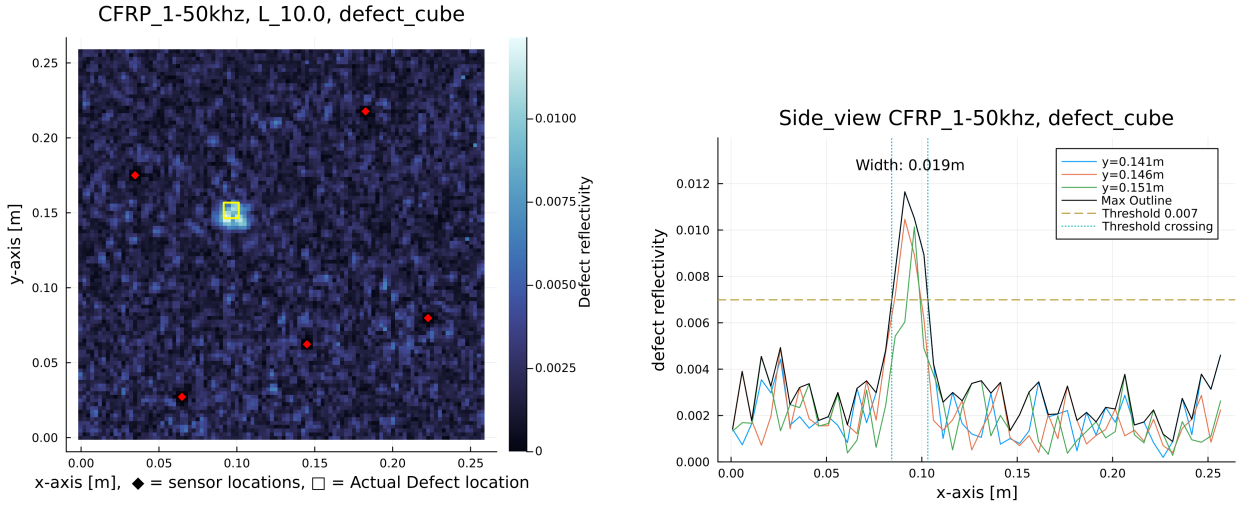
The result demonstrates successful localization of the $1 \times 1 \times 1\,\text{cm}^3$ iron cube using only sparse measurements at the five transducer locations. The particle velocity data was bandpass filtered to 1–50 kHz and processed via the Tikhonov-regularized inversion described in Section 3.7.

Figure 5b provides cross-sectional views along the x-axis. Slices exceeding 0.6 times the maximum amplitude are retained, and their envelope is drawn. This threshold identifies the localization width: the defect signature has a half-width of approximately 2 cm.

5. Results - Simulations

The method was validated using commercial finite-element simulations of a 9 mm thick rectangular aluminum plate, with defects modeled as localized reductions in density.

Case A: Figure 6 shows a tapered circular lower-density inclusion of 1.5 cm diameter with relative density 0.2, demonstrating accurate localization in a controlled setting. The repetition period is 2 ms, with 5 sensors in a similar configuration, 20% Gaussian RMS noise, and a 0–50 kHz low-pass filter matching the real-world example. A 50 kHz Ricker wavelet is used as the driving pulse instead of 80 kHz, which should not significantly change the results.

CFRP_1-50khz, L_10.0, defect_cube

Side_view CFRP_1-50khz, defect_cube

(a) Reconstructed magnitude of the defect vector $|\vec{\mathbf{d}}|$ in the 1–50 kHz band. Red diamonds mark the five transducer locations. The yellow square indicates the actual location where the iron cube was bonded. The black regions around transducers are the unpenalized exclusion zones from the regularization.

(b) Cross-sectional profiles along the x-axis through the reconstructed defect (left panel). Colored envelopes show slices with amplitude exceeding 0.6 times the maximum. The localization width is estimated from the 0.6 amplitude threshold, yielding a half-width of approximately 2 cm.
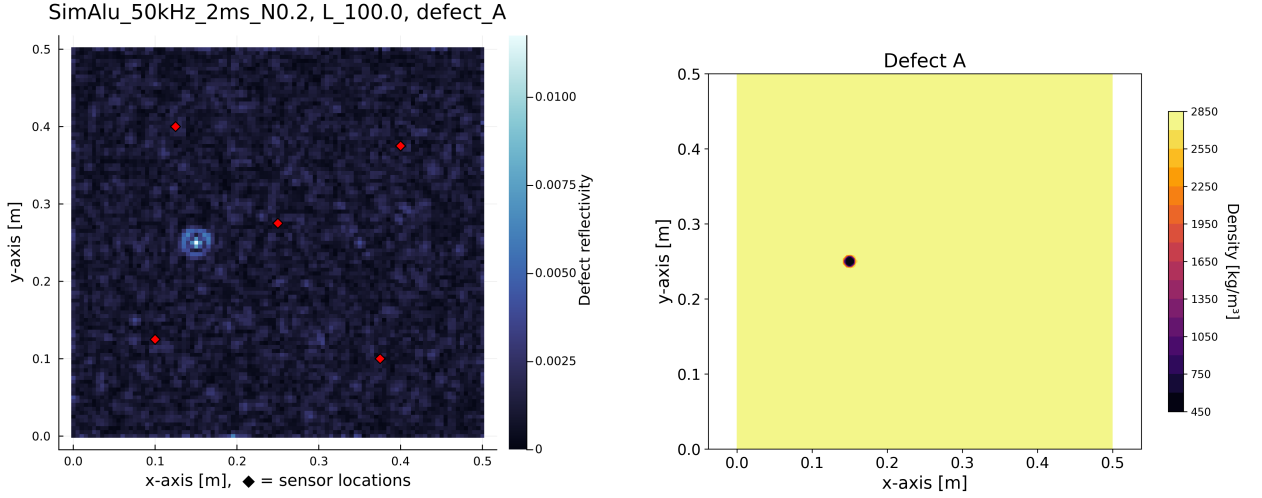
Figure 5: Defect localization results in the 1–50 kHz band using sparse transducer measurements. Left: full 2D reconstruction showing sub-wavelength localization of the defect. Right: cross-sectional analysis quantifying the localization width.

Case A5B_1: Figure 7 contains two tapered inclusions of 1.5 cm and 5 cm diameter at relative density 0.2, using the same parameters as before. It showcases the ability of the method to discern multiple defects simultaneously and larger shapes, despite internally assuming single scattering. The reconstruction, however, shows degradation in the form of significant background artifacts, which appear when the scenario departs from cases well described by single scattering.

Case A5B_2: In Figure 8a, the same defect as in 7 is simulated with a 5 ms period and 0–100 kHz frequency range. The algorithm therefore has access to five times more temporal information than in the previous cases. We observe a marked increase in defect reconstruction fidelity and a decrease in background artifacts. Although the parameters are not isolated, comparing the reconstruction of the small defect with that of Figure 6 shows increased localization accuracy resulting from the higher available frequencies. The longer period, and thus additional information, appears to help in compensating multiple scattering effects and reducing background artifacts. This interpretation is supported by many additional simulations with varied parameters discussed in [32].

Case ECHO: Figure 8b provides a proof of concept that the method can operate using only one sensor. In this case, a single transducer is active as emitter and simultaneously acts as the only sensor, essentially a pulse-echo configuration. The data are bandpass filtered to 0–100 kHz with a 5 ms period and 10% RMS noise. All other parameters are the same as in the other simulation cases. The reconstructed defect closely resembles the small defect of Figure 8a, rather than 6a, indicating that localization accuracy is primarily determined by data frequency rather than the number of sensors and thus the amount of data. However, more complex defects such as 7b (not shown here) are evaluated much worse in this echo configuration. It is more susceptible to noise and works significantly worse at lower frequencies. These findings align with the description of a similar problem in [17], where increased sensor counts decrease "contrast" (called "background artifacts" here) but do not increase resolution as higher frequencies do. The problem statement is very similar to that of [11, 10], providing a close comparison to different approaches. Evaluation attempts using real world data did not yield interpretable results, which is in line with the simulations performing poorly as well with the same parameters, as the low frequency and period length offers very little information.
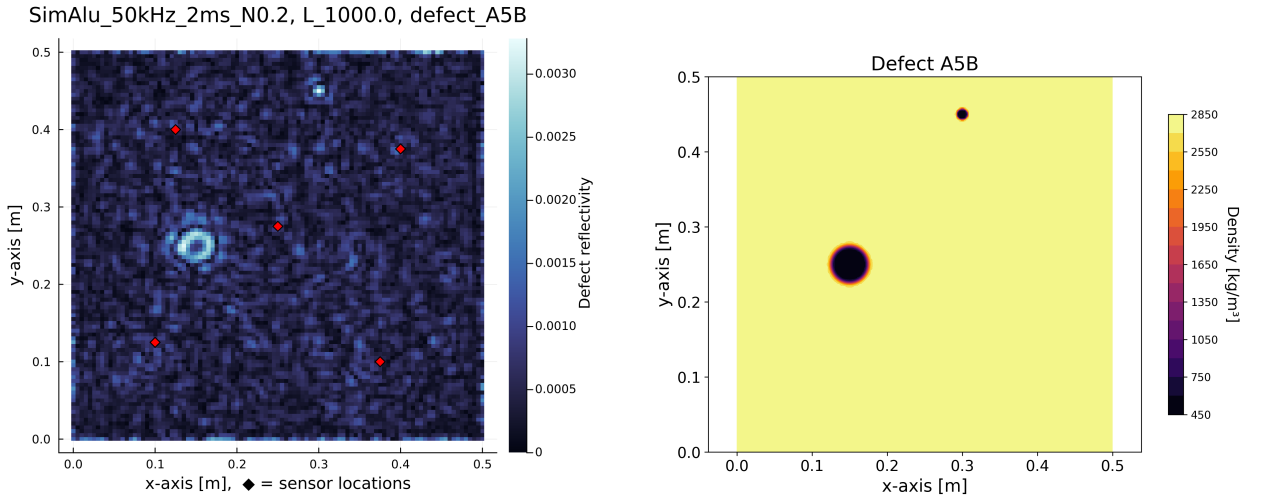
Further details and additional simulation examples are documented in [32].

SimAlu_50kHz_2ms_N0.2, L_100.0, defect_A

(a) Reconstructed defect amplitude for simulated case A in the 0–50 kHz band, showing accurate localization of a single 1.5 cm inclusion under 20% RMS noise.

(b) Ground-truth density map for case A, with a tapered circular lower-density inclusion of 1.5 cm diameter and relative density 0.2.

Figure 6: Simulation case A with a single small inclusion. Left: reconstructed defect amplitude obtained with the empirical-operator inversion. Right: corresponding ground-truth density map.

SimAlu_50kHz_2ms_N0.2, L_1000.0, defect_A5B

(a) Reconstructed defect amplitude for simulated case A5B with two inclusions, resolving the 1.5 cm and 5 cm defects but showing increased background artifacts.
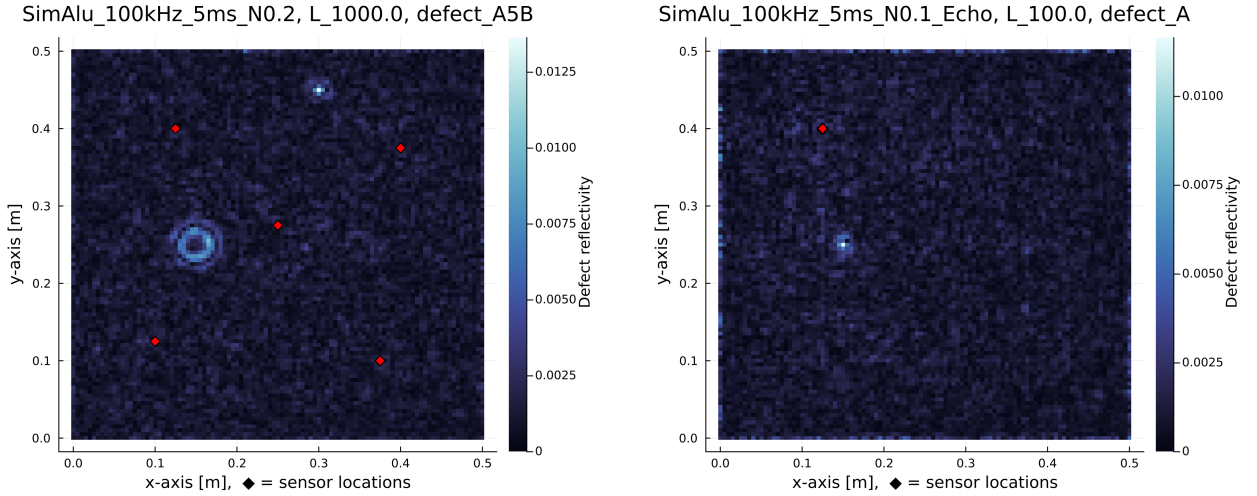
(b) Ground-truth density map for case A5B, containing two tapered circular lower-density inclusions with diameters of 1.5 cm and 5 cm at relative density 0.2.

Figure 7: Simulation case A5B with two inclusions. Left: reconstruction illustrating simultaneous localization of both defects and the emergence of background artifacts. Right: ground-truth density map used as reference.

6. Discussion

The reconstructed defect has a half-width of approximately 2 cm compared to a wavelength of $\lambda_{50} \approx 8$ cm at 50 kHz (Figure 3b), yielding sub-wavelength localization. This is notably below the wavelength scale. The reasons for this property have prompted considerable discussion, which are discussed in A.8.

The absolute pixel values in Figure 5a should be interpreted as relative indicators of defect location rather than quantitative scattering amplitudes, as the regularization parameter λ significantly influences amplitude scaling. Testing

SimAlu_100kHz_5ms_N0.2, L_1000.0, defect_A5B

SimAlu_100kHz_5ms_N0.1_Echo, L_100.0, defect_A

(a) Reconstruction of case A5B using 5 ms period and 0–100 kHz bandwidth, demonstrating reduced background artifacts and sharper localization compared to Fig. 7.

(b) Single-transducer pulse-echo reconstruction of the small defect from case A (Fig. 6), using 0–100 kHz bandwidth with 10% RMS noise.

Figure 8: Simulation cases with extended frequency range and reduced sensor count. Left: case A5B_2 at 0–100 kHz shows improved reconstruction fidelity. Right: pulse-echo configuration (case ECHO) successfully localizes defect A using a single transducer.

with extended frequency ranges showed that the 1–80 kHz band yields only modest improvements over 1–50 kHz, while extending to 1–150 kHz causes severe degradation. This likely stems from imperfect LDV realignments during defect measurements, an issue that should disappear entirely when using transducers for monitoring (Appendix A.4). The unpenalized regions around transducers (Section 3.7) suppress phantom defects by absorbing pulse variations locally, demonstrating the method's robustness to experimental imperfections.

The experimental defect is an adhered metal cube, which differs from realistic CFRP damage such as delaminations. Delamination detection has been explored with mixed results in [32], with room for improvement. However, the cube defect serves as a useful proxy for contact-based applications, and the computational efficiency after calibration (Appendix A.3) suggests viability for both frequent automated SHM and low-cost touchscreen implementations [17].

Although not explicitly explored in this paper, previous simulation work documented in [32] indicated several limitations of the approach. Large defects with a relative size of order ≈ 0.1 of the system become hard to resolve, likely because the single scattering approximation starts to break down. The reconstruction quality also depends on the defect shape, and while small defects can be localized well below the wavelength, their shape cannot be recovered if they are much smaller than the wavelength.

7. Conclusion

This paper presented and experimentally validated an empirical, fully vectorized linear-operator framework for inverse scattering and structural health monitoring. Using bonded piezoelectric transducers and a one-time LDV calibration scan, we constructed source–receiver impulse-response operators on a discrete periodic time axis, represented propagation as circular convolution diagonalized by the DFT, and posed defect localization as a Tikhonov-regularized linear inverse problem. On an anisotropic CFRP plate, an adhered 1 cm^3 iron cube was localized from sparse measurements at the transducer locations with sub-wavelength resolution ($\approx$2cm localization accuracy at a minimum wavelength of 8cm), concentrating computation in the one-time calibration while keeping subsequent monitoring lightweight.

The framework is general and modular: it does not rely on a detailed forward model and can, in principle, be extended to other defect bases, sensing layouts, and wave-bearing media, provided approximate linearity and time

invariance. Current limitations, such as the single-scattering assumption, a simple defect basis, and reliance on LDV for calibration point to natural future work toward more complex scattering regimes and fully transducer-based implementations.

While the method presented here is intended as a practical route toward cost-effective, frequent SHM, the broader point concerns how we choose to describe and interpret a physical system. Rather than insisting on a fully resolved forward model of every underlying quantity, we focus on the relationships between measured signals and let those relationships carry most of the modeling burden. We deliberately reshape the description: although physical time is not periodic, we can design an experiment that behaves as if it were, and then exploit the computational and experimental advantages this offers. In this description, many details that are usually modeled separately—transducer coupling, attenuation, and the interplay of multiple wave modes—are absorbed into the empirical operators by construction, or can be handled with minor adjustments. This perspective can extend beyond the linear-operator framework used here. In SHM and NDT, periodic time can often be enforced experimentally, and the abstract treatment of measured quantities aligns naturally with recently popular machine-learning approaches. Combining such experimental designs with data-driven models may provide a general route to robust, low-maintenance monitoring or detection systems in different fields.

Working effectively in the 1–50 kHz band validates the empirical-operator concept, even with practical imperfections such as pulse-shape drift and measurement misalignment. The robustness in this band supports our initial hypothesis: circumventing detailed forward models in favor of empirical operators leads to numerically robust properties in the detection algorithm, allowing imperfections to be absorbed into the interpretation of the measured quantities themselves. By removing explicit spatial information entirely (the algorithm does not know about the spatial relations between each grid point), it naturally removes restrictions caused by the frequency-to-pulse-width relation, allowing us to work at low frequencies, which in turn leads to numerical robustness.

A. Appendix

A.1. Longitudinal Velocity Components

In both simulation and real world experiments, only the out of plane components have been used. The real world setup used an LDV capable of also recording velocities in all three space directions. The method should in theory be able to use any of the three dimensions, or their sum as the measured quantities. This was not explored during the Simulation work, and in the real world experiment, these components showed high noise ratios, as well as many "dead" grid points without measurements for unknown systematic reasons, yielding non interpretable results. As such, we could not verify that this method extends to longitudinal wave components.
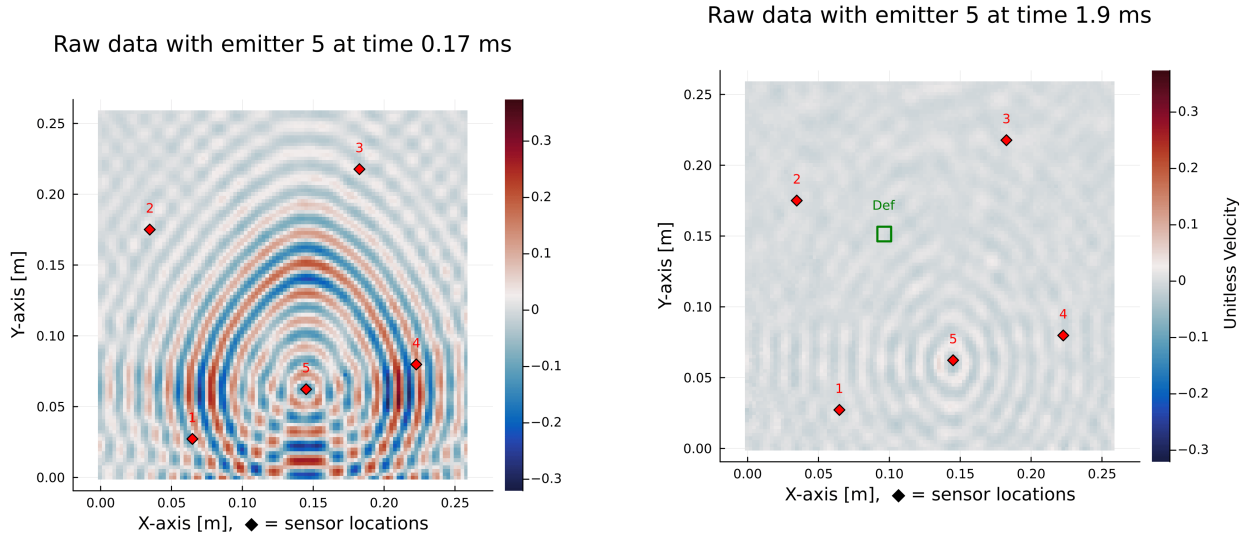
Exploration of this property could be practical in the case of pursuit of a practical SHM implementation. If the hypothesis holds that the sum of all three velocity components is a valid quantity for this method, in the case of curved surfaces, would remove the need to compute the out-of-plane component at various directions. The result would be a simplified implementation where the three-component velocity at every grid point could be fed directly from the LDV into the algorithm without accounting for the orientation of the surface at any given point. Further reading: [32].

A.2. Low Frequency data

The results presented in the main paper employ a 1–50 kHz bandpass filter, which differs significantly from the unfiltered calibration data shown in Figure 2. Figure 9a shows the same acquisition time point, but after lowpass filtering to 50 kHz. The pulse duration expands dramatically, becoming so long that it wraps around within the periodic time window. At the end of the 2 ms period ($t \approx 1.9$ ms), the pulse from the next repetition is already visible (Figure 9b). This behavior illustrates a key strength of the framework: the algorithm does not require short, well-separated pulses. The periodic time treatment is therefore not just a computational convenience but is fundamentally embedded in the mathematics of the inverse problem.

A.3. Computational performance

In the implementation used in this paper, the global system matrix $\mathcal{L}_{\text{full}}$ from equation 14 is formed explicitly and inverted in a Tikhonov sense via $(\mathcal{L}^T\mathcal{L} + \lambda\Gamma)^{-1}\mathcal{L}^T$. For a matrix of size $n \times m$ with measurements n and defect parameters m (equals grid size in our case), memory scales as $\mathcal{O}(nm)$ and the inversion cost as $\mathcal{O}(nm^2)$. Adding measurements is therefore comparatively cheap, whereas enlarging the defect space is the dominant computational bottleneck. On a

Raw data with emitter 5 at time 0.17 ms

Raw data with emitter 5 at time 1.9 ms

(a) CFRP plate response at $t = 0.17$ ms, bandpass filtered to 1–50 kHz. Transducer 5 is active. Compared to the unfiltered snapshot in Figure 2, the pulse is significantly broadened due to the lowpass filtering.

(b) Same setup at $t = 1.9$ ms, near the end of the 2 ms period. The pulse tail from the current repetition is still visible, and the pulse from the next repetition (nominally starting at $t = 0.12$ ms) is already present, demonstrating the wraparound inherent in the periodic time treatment.

Figure 9: Effect of 1–50 kHz bandpass filtering on the transducer pulse shape in the periodic time framework.

standard laptop with 16 GB RAM (about 9 GB effectively usable) and an Intel Gen13 i7 CPU, practical limits are matrices of order $10^4 \times 3 \times 10^4$ in Float32 (~1.2 GB for the main matrix), with additional overhead from temporary work arrays. For the experimental CFRP case studied here ($\approx 10^4$ defect parameters and $\approx 10^3$ measurements), the one-time inversion of $\mathcal{L}_{\text{full}}$ takes about 17 s. The empirical impulse responses (Section 3.4) are obtained in roughly 4 s and scale linearly in grid size and measurement points, so they remain inexpensive compared to the inversion as the scale increases. The subsequent evaluations for new measurement vectors reduce to a single matrix–vector multiplication and take around 3–5 ms in the presented case. From a computational perspective, this separation between a moderately expensive calibration step and very fast evaluation makes the method potentially viable as a low-cost, touchscreen application as in [17]. The evaluation does not have any memory requirements, potentially allowing frequent automated SHM on a simple system.

A.4. Frequency content and dispersion

Figures 3 suggest phase velocities that increase with frequency and reach values of order 10km/s at the upper end of the measured band. A theoretical Lamb-mode estimate[12] using rough CFRP parameters places the high-frequency A0 branch near 3.8 km/s. Both the empirical and theoretical numbers should be considered approximate.

The empirical estimates may be affected by measurement noise, limited angular sampling, and small alignment errors between calibration and monitoring. Conversely, the theoretical Lamb-mode calculation is only a rough ballpark because it assumes isotropic, homogeneous material properties and does not account for the plate's anisotropy or layup. Hence, discrepancies between the two are to be expected and can be substantial. Neither approach alone provides a definitive "ground truth."

A bigger concern may be that manually computing dx/dt on Figure 3b, which corresponds more to the group velocity, yields a result of roughly 1700m/s.

For the purposes of this paper we only use phase-velocity/wavelength estimates as a rough reference to assess whether the observed localization is below the order-of-magnitude wavelength. At 50 kHz, the corresponding wavelengths are on the order of a few centimeters, and the observed localization ($\approx$2 cm) remains smaller than those wavelengths. Given that this comparison is only qualitative, we do not pursue a detailed velocity validation here.

In the real world example, the algorithm shows limited additional benefit from including higher-frequency data, even though the measured wave spectrum extends well beyond 50 kHz, as expected from the 80 kHz central frequency of the transmitted pulses and confirmed by measurements at multiple locations on the plate. This behavior deviates from previous simulation results obtained using the same method (Appendix 5, [32]).

Analysis of the 100–150 kHz band alone yields poor results, indicating that this frequency range carries no useful information for defect localization in the current setup. The 1–50 kHz range working similarly well to 1–80 kHz is especially interesting considering that the system matrix to be solved in equation 14 has dimensions 1000×10816. The inversion problem is highly underdetermined by a factor of over 10, meaning the additional information should be valuable, but is not.

Since the degradation at higher frequencies in not present in the simulated results 5, a key source of degradation at higher frequencies is likely misalignment between the calibration and monitoring phases. During calibration, the LDV scans a dense 104×104 grid. During monitoring, the LDV measures at transducer locations only, and realignment relies on visual cues, introducing small spatial offsets. Such misalignments couple strongly to phase information at shorter wavelengths. Notably, this alignment issue would be eliminated entirely if monitoring were performed using the transducers themselves as receivers rather than the LDV, as discussed in Section A.5.

Alternatively, the discrepancy may stem from assumptions in the problem formulation. In Section 3.5, defects are assumed to exhibit a delta-like response, implying instantaneous, frequency-independent reflection. In the simulation study, defects were modeled as changes in density, whereas the experimental defect, an adhered metal cube, more closely represents a change in stiffness, for which this assumption may be less valid.

Therefore, restricting the frequency band may be advantageous: Although fewer data are used, the underlying assumptions only need to hold over a narrower frequency range. However, the current experimental setup does not allow these effects to be isolated, so no definitive conclusion can be drawn.

A.5. Piezoelectric Measuring

This section will likely have to be moved to a future work section or similar A fully transducer-based implementation could proceed as follows: For each transducer location, two transducers are placed close together, one acting as the transmitter, and the other as the sensor. During calibration, a transmitting transducer emits a periodic pulse while an LDV scans the object. The measurements from the sensing transducer are added to the LDV data and treated as an additional grid point. In the code, the sensing transducer's measurement is assigned to the emitter location, so any coupling effects are absorbed into the object properties, potentially allowing the use of inexpensive transducers with poor coupling.

Notes: Thick, cube-shaped transducers should be avoided, as their stiffness locally alters the plate and makes measurement at or by the transducer impossible. Always use flat, plate-like ceramic transducers relative to the plate thickness.

It is important to note that the physical location of the emitting transducer and the modeled transmitter location may not coincide. This is intentional and consistent with the approach in this paper, since the LDV does not scan exactly at the transducer positions. Whilal and modeled transducer locations is theoretically possible, it quickly becomes unstable at separations of a few centimeters. Using one emitter and multiple nearby sensing transducers, treating each sensor as an emitter in the model, may be feasible, but the practical benefit is likely limited.

A.6. Generalization to arbitrary defect bases

As mentioned in Section 3.5 and applied in Section 3.6, we assumed the defect to act as a perfect reflector of form $\vec{e}_0$. In general this assumption does not hold for more complicated defects, such as delaminations in fiber-reinforced materials. In this case, using a simulation with a defect at a known location, one can compute the response nature through similar means to those described in Sections 3.6 and 3.7. Assuming we have obtained empirical defect vectors for two defect types of interest, $\vec{b}_1$ and $\vec{b}_2$, we can implement these two vectors as a basis using a projector matrix P:

$$P := \begin{bmatrix} \vec{b}_1 & \vec{b}_2 \end{bmatrix} \tag{17}$$

Replacing $\vec{e}_0$ in 12, we obtain

$$L_{ij} := \begin{bmatrix} G_{i1}G_{1j}S_jP & | & G_{i2}G_{2j}S_jP & | & \cdots & | & G_{iN}G_{Nj}S_jP \end{bmatrix}, \tag{18}$$

as well as an adjustment to the full defect vector $\mathbf{d}$ to hold two parameters per location.

$$\mathbf{d} := \begin{bmatrix} d_{1,1} \\ d_{1,2} \\ d_{2,1} \\ \vdots \\ d_{N,2} \end{bmatrix} \tag{19}$$

where for $d_{k,b}$, k denotes the grid location, and b the basis vector at that location.

This approach is not used in this paper, as we continue using a delta-like simplifies defect. Experiments in simulation work so far has not yielded many useful bases that significantly increased performance. Especially considering the computational costs associated with increasing the defect space, as well as since we are already working in highly underdetermined systems in this paper. See [32] for further discussions into different defect bases.

A.7. Sensor Configurations

The sensor configuration used in this paper as described in section 3.6 are chosen as s [[1,2], [1,3], [1,4], [1,5], [2,3], [2,4], [2,5], [3,4], [3,5], [4,5]]. For the echo configuration in Figure 8b, it is [[1,1]]. The choice of the 5-sensor system is motivated by avoiding symmetric sets to be included, such as [[1,2],[2,1]], as due to the reciprocity assumption, do not provide additional significant useful information. Testing confirmed this to be the case.

In hindsight, it would likely be better to use a basis layout such as [[1,2],[1,3],[2,3],[2,4],[3,4],...] to treat all emitters equally importantly. This was thought of too late, but testing afterwards revealed no noticeable improvements when using such a configuration. Therefore, the results were kept.

The inclusion of a full set of measurements including self-measurements such as ([1,1],[2,2] etc.) should in theory improve the results, but testing shows a tendency to decrease the result quality, which is odd, given the single pulse cases 8b do work, therefore the information should not be useless.

A.8. Sub-Wavelength localization discussions

and it remains challenging to provide a concise explanation, especially since it is difficult to demonstrate why something does *not* occur. Based on the mathematical methodology used which does not rely on explicit spatial information, there appears to be no inherent restriction enforcing a wavelength limit. In contrast, other methods often have such restrictions, typically due to the need to reconstruct measured waves in space. For example, [11] describes a method with this limitation, though it is not explicitly discussed there.

However, in the simulation study, a decrease in resolution is observed at lower frequencies, which suggests that the method is not entirely independent of wavelength-related limits. The discussion is complicated by the fact that changing the frequency bandwidth simultaneously affects three factors: the maximum frequency, the amount of information available due to the system matrix shape (see Eq. 14), and increased susceptibility to standard norm-based regularization, which can smear the result because neighboring points respond more similarly at longer wavelengths. For all intents and purposes, the method does have a resolution limitation as a function of frequency, but it is also dependent on other variables, without a hard cutoff based on frequency alone, such as with the Nyquist sampling theorem. Given the proof-of-concept nature of this paper, we refrain from exploring this topic in depth, simply noting that it is possible to isolate each variable to obtain definite answers if desired

References

[1] , . 4. Computational Aspects: Regularization Methods. pp. 53–83. URL: https://epubs.siam.org/doi/abs/10.1137/1.9780898718836.ch4, doi:10.1137/1.9780898718836.ch4, arXiv:https://epubs.siam.org/doi/pdf/10.1137/1.9780898718836.ch4.

[2] , . 5. Getting Serious: Choosing the Regularization Parameter. pp. 85–107. URL: https://epubs.siam.org/doi/abs/10.1137/1.9780898718836.ch5, doi:10.1137/1.9780898718836.ch5, arXiv:https://epubs.siam.org/doi/pdf/10.1137/1.9780898718836.ch5.

[3] Bazulin, E., Goncharsky, A., Romanov, S., Seryozhnikov, S., 2019. Inverse problems of ultrasonic tomography in nondestructive testing: Mathematical methods and experiment. Russian Journal of Nondestructive Testing 55, 453–462. doi:10.1134/S1061830919060020.

[4] Calomfirescu, M., 2008. Lamb Waves for Structural Health Monitoring in Viscoelastic Composite Materials. Science-Report aus dem Faserinstitut Bremen, Logos-Verlag. URL: https://books.google.ch/books?id=_p6muhkbVB0C.

[5] Cawley, P., 2002. Practical long range guided wave inspection - applications to pipes and rail, Chennai.

[6] Celli, P., Porfiri, M., 2022. The detection matrix as a model-agnostic tool to estimate the number of degrees of freedom in mechanical systems and engineering structures. Chaos: An Interdisciplinary Journal of Nonlinear Science 32. URL: http://dx.doi.org/10.1063/5.0083767, doi:10.1063/5.0083767.

[7] Chen, S., Thompson, A., Dodwell, T., Hallett, S., Belnoue, J., 2025. A comparison between robust design and digital twin approaches for non-crimp fabric (ncf) forming. Composites Part A: Applied Science and Manufacturing 193, 108864. URL: https://www.sciencedirect.com/science/article/pii/S1359835X25001587, doi:https://doi.org/10.1016/j.compositesa.2025.108864.

[8] Chia, C.C., Lee, S.Y., Harmin, M.Y., Choi, Y., Lee, J.R., 2023. Guided ultrasonic waves propagation imaging: a review. Measurement Science and Technology 34, 052001. URL: https://iopscience.iop.org/article/10.1088/1361-6501/acae27, doi:10.1088/1361-6501/acae27.

[9] Derusova, D.A., Vavilov, V.P., Druzhinin, N.V., Shpil'noi, V.Y., Pestryakov, A.N., 2022. Detecting defects in composite polymers by using 3d scanning laser doppler vibrometry. Materials 15. URL: https://www.mdpi.com/1996-1944/15/20/7176, doi:10.3390/ma15207176.

[10] Draeger, C., Fink, M., 1997. One-channel time reversal of elastic waves in a chaotic 2d-silicon cavity. Phys. Rev. Lett. 79, 407–410. URL: https://link.aps.org/doi/10.1103/PhysRevLett.79.407, doi:10.1103/PhysRevLett.79.407.

[11] Ebrahimkhanlou, A., Salamone, S., 2017. Acoustic emission source localization in thin metallic plates: A single-sensor approach based on multimodal edge reflections. Ultrasonics 78, 134–145. doi:10.1016/j.ultras.2017.03.006.

[12] Francisco Rotea, l., . URL: https://github.com/franciscorotea/Lamb-Wave-Dispersion?tab=readme-ov-file.

[13] Fu, Y., Yao, X., 2022. A review on manufacturing defects and their detection of fiber reinforced resin matrix composites. Composites Part C: Open Access 8, 100276. URL: https://www.sciencedirect.com/science/article/pii/S266668202200041X, doi:https://doi.org/10.1016/j.jcomc.2022.100276.

[14] Fuhry, M., Reichel, L., 2012. A new Tikhonov regularization method. Numerical Algorithms 59, 433–445. URL: https://doi.org/10.1007/s11075-011-9498-x, doi:10.1007/s11075-011-9498-x.

[15] Golub, G., Heath, M., Wahba, G., 1979. Generalized cross-validation as a method for choosing a good ridge parameter. Technometrics 21, 215–223. doi:10.1080/00401706.1979.10489751.

[16] Han, S., Li, Q., Cui, Z., Xiao, P., Miao, Y., Chen, L., Li, Y., 2024. Non-destructive testing and structural health monitoring technologies for carbon fiber reinforced polymers: a review. Nondestructive Testing and Evaluation 39, 725–761. URL: https://doi.org/10.1080/10589759.2024.2324149, doi:10.1080/10589759.2024.2324149, arXiv:https://doi.org/10.1080/10589759.2024.2324149.

[17] Ing, R.K., Quieffin, N., Catheline, S., Fink, M., 2005. In solid localization of finger impacts using acoustic time-reversal process. Applied Physics Letters 87, 204104. URL: https://doi.org/10.1063/1.2130720, doi:10.1063/1.2130720. _eprint: https://pubs.aip.org/aip/apl/article-pdf/doi/10.1063/1.2130720/13168422/204104_1_online.pdf.

[18] Jankauskas, A., Mažeika, L., 2011. Wind turbine blade analysis using ultrasonic guided waves. URL: https://www.ndt.net/article/CompNDT2011/papers/15_Jankauskas.pdf.

[19] Kosova, F., Özkan Altay, Özgür Ünver, H., 2025. Structural health monitoring in aviation: a comprehensive review and future directions for machine learning. Nondestructive Testing and Evaluation 40, 1–60. URL: https://doi.org/10.1080/10589759.2024.2350575, doi:10.1080/10589759.2024.2350575, arXiv:https://doi.org/10.1080/10589759.2024.2350575.

[20] Kudela, P., Polish Academy of Sciences (PAS), Fiborek, P., Polish Academy of Sciences (PAS), Ostachowicz, W.M., 2024. Wave Propagation for Structural Health Monitoring (WaveProSHM): open software with GUI. e-Journal of Nondestructive Testing 29. URL: https://www.ndt.net/search/docs.php3?id=29639, doi:10.58286/29639.

[21] Love, A.E.H., 1888. The small free vibrations and deformation of a thin elastic shell. Philosophical Transactions of the Royal Society of London. A 179, 491–546. URL: http://www.jstor.org/stable/90527.

[22] Mustapha, S., Saad, D.M., Fakih, M.A., Yuan, F.G., 2024. Composite sandwich structures: Damage detection and assessment using ultrasonic guided waves, in: Structural Health Monitoring/management (SHM) in Aerospace Structures. Elsevier, pp. 55–99. URL: https://linkinghub.elsevier.com/retrieve/pii/B9780443154768000162, doi:10.1016/B978-0-443-15476-8.00016-2.

[23] Olisa, S.C., Khan, M.A., Starr, A., 2021. Review of Current Guided Wave Ultrasonic Testing (GWUT) Limitations and Future Directions. Sensors 21, 811. URL: https://www.mdpi.com/1424-8220/21/3/811, doi:10.3390/s21030811.

[24] Ostachowicz, W., Kudela, P., Radzieński, M., 2024. Identification of composite material properties by elastic wave propagation methods, in: Structural Health Monitoring/management (SHM) in Aerospace Structures. Elsevier, pp. 389–408. URL: https://linkinghub.elsevier.com/retrieve/pii/B9780443154768000010, doi:10.1016/B978-0-443-15476-8.00001-0.

[25] Park, B., Sohn, H., Malinowski, P., Ostachowicz, W., 2017. Delamination localization in wind turbine blades based on adaptive time-of-flight analysis of noncontact laser ultrasonic signals. Nondestructive Testing and Evaluation 32, 1–20. URL: https://www.tandfonline.com/doi/full/10.1080/10589759.2015.1130828, doi:10.1080/10589759.2015.1130828.

[26] Raghavan, A., Cesnik, C.E.S., 2007. Review of Guided-wave Structural Health Monitoring. The Shock and Vibration Digest 39, 91–114. URL: http://svd.sagepub.com/cgi/doi/10.1177/0583102406075428, doi:10.1177/0583102406075428.

[27] Thomsen, H.R., Van Manen, D.J., Baettig, S., Brauner, C., Gebraad, L., Boehm, C., 2024. The W-Scan: leveraging guided waves to create digital twins for non- destructive evaluation of composite materials, Brugg-Windisch.

[28] Tikhonov, A.N., 1963. On the solution of ill-posed problems and the method of regularization. Dokl. Akad. Nauk SSSR 151, 501–504. URL: https://www.mathnet.ru/eng/dan/v151/i3/p501. english translation available via MathNet.Ru.

[29] Wan, L., Ismail, Y., Sheng, Y., Ye, J., Yang, D., 2023. A review on micromechanical modelling of progressive failure in unidirectional fibre-reinforced composites. Composites Part C: Open Access 10, 100348. URL: https://www.sciencedirect.com/science/article/pii/S266668202300004X, doi:https://doi.org/10.1016/j.jcomc.2023.100348.

[30] Waqar, M., Memon, A.M., Sabih, M., Alhems, L.M., 2024. Composite pipelines: Analyzing defects and advancements in non-destructive testing techniques. Engineering Failure Analysis 157, 107914. URL: https://www.sciencedirect.com/science/article/pii/

S1350630723008683, doi:https://doi.org/10.1016/j.engfailanal.2023.107914.

[31] Wilcox, P., Monkhouse, R., Lowe, M., Cawley, P., 1998. The Use of Huygens' Principle to Model the Acoustic Field from Interdigital Lamb Wave Transducers. Springer US, Boston, MA. pp. 915–922. URL: https://doi.org/10.1007/978-1-4615-5339-7_118, doi:10.1007/978-1-4615-5339-7_118.

[32] Wueest, R., 2025. Github repository to the code, as well as further documentation. https://github.com/Fiiidch/Fully-Vectorized-Linear-Operator-Formulation-for-Inverse-Scattering-Problems.

[33] Yawn, K.R., Drake, T.E., Osterkamp, M.A., Chuang, S.Y., Acres, P., Thomas, M., Kaiser, D., Marquardt, C., Filkins, B., Lorraine, P., Martin, K., Miller, J., 1999. Large-Scale Laser Ultrasonic Facility for Aerospace Applications. Springer US, Boston, MA. pp. 387–393. URL: https://doi.org/10.1007/978-1-4615-4791-4_48, doi:10.1007/978-1-4615-4791-4_48.

[34] Yu, S., Luo, K., Fan, C., Fu, K., Wu, X., Chen, Y., Zhang, X., 2025. Advancing spacecraft safety and longevity: A review of guided waves-based structural health monitoring. Reliability Engineering & System Safety 254, 110586. URL: https://linkinghub.elsevier.com/retrieve/pii/S0951832024006574, doi:10.1016/j.ress.2024.110586.